Helmholtz-Zentrum Dresden-Rossendorf (HZDR)

HELMHOLTZ ZENTRUM
DRESDEN ROSSENDORF

Antimonite binding to natural organic matter: Spectroscopic evidence from a mine water impacted peatland

Besold, J.; Eberle, A.; Noël, V.; Kujala, K.; Kumar, N.; Scheinost, A.; Lezama Pacheco, J.; Fendorf, S.; Planer-Friedrich, B.;

Originally published:

August 2019

Environmental Science & Technology 53(2019), 10782-10802

DOI: https://doi.org/10.1021/acs.est.9b03924

Perma-Link to Publication Repository of HZDR:

https://www.hzdr.de/publications/Publ-29265

Release of the secondary publication
on the basis of the German Copyright Law § 38 Section 4.

"Antimonite Binding to Natural Organic Matter: Spectroscopic Evidence from a Mine Water Impacted Peatland"

Johannes Besold[1], Anne Eberle[1], Vincent Noël[2], Katharina Kujala[3], Naresh Kumar[4,5], Andreas C. Scheinost[6], Juan Lezama Pacheco[7], Scott Fendorf[5] and Britta Planer-Friedrich[1]*

[1] Department of Environmental Geochemistry, Bayreuth Center for Ecology and Environmental Research (BAYCEER), Bayreuth University, 95440 Bayreuth, Germany

[2] Stanford Synchrotron Radiation Lightsource, SLAC National Accelerator Laboratory, Menlo Park, CA 94025, United States

[3] Water Resources and Environmental Engineering Research Unit, University of Oulu, FI-90014, Oulu, Finland

[4] Department of Geological Sciences, School of Earth, Energy, and Environmental Sciences, Stanford University, Stanford, CA 94305, USA.

[5] Department of Environmental Geosciences, University of Vienna, 1090 Vienna, Austria

[6] The Rossendorf Beamline (ROBL) at ESRF, 38043 Grenoble, France and Helmholtz-Zentrum Dresden-Rossendorf (HZDR), Institute of Resource Ecology, Bautzner Landstraße 400, 01328 Dresden, Germany

ABSTRACT

Peatlands and other wetlands are sinks for antimony (Sb). Solid natural organic matter (NOM) has thus been suggested to play an important role in controlling Sb binding in wetland sediments. However, direct spectroscopic evidence for this sequestration mechanism in natural peat samples is still lacking. In order to investigate Sb binding in peat, we sampled and characterized three profiles up to a depth of 80 cm in an Sb-impacted peatland in northern Finland. We used bulk *K*-edge X-ray absorption spectroscopy to study the speciation of Fe, S and Sb in the peat solid phase. Additionally, we determined the aqueous speciation of Sb in surface and pore waters. Based on linear combination fittings of extended X-ray absorption fine structure spectra, we found that Sb associated to the solid-phase is up to 100% coordinated to organic phenol and/or thiol groups. Even in the presence of iron, organically-bound Sb(III) was the dominant fraction in all peat profiles and across all depths. While aqueous antimonite concentrations were low, Sb(III) species were dominating solid-phase speciation, suggesting a high reactivity of Sb(III) towards peat surfaces. Our findings therefore confirm that Sb binding to solid NOM acts as an important sequestration mechanism under reducing conditions in NOM-rich wetlands.

35 TOC
36

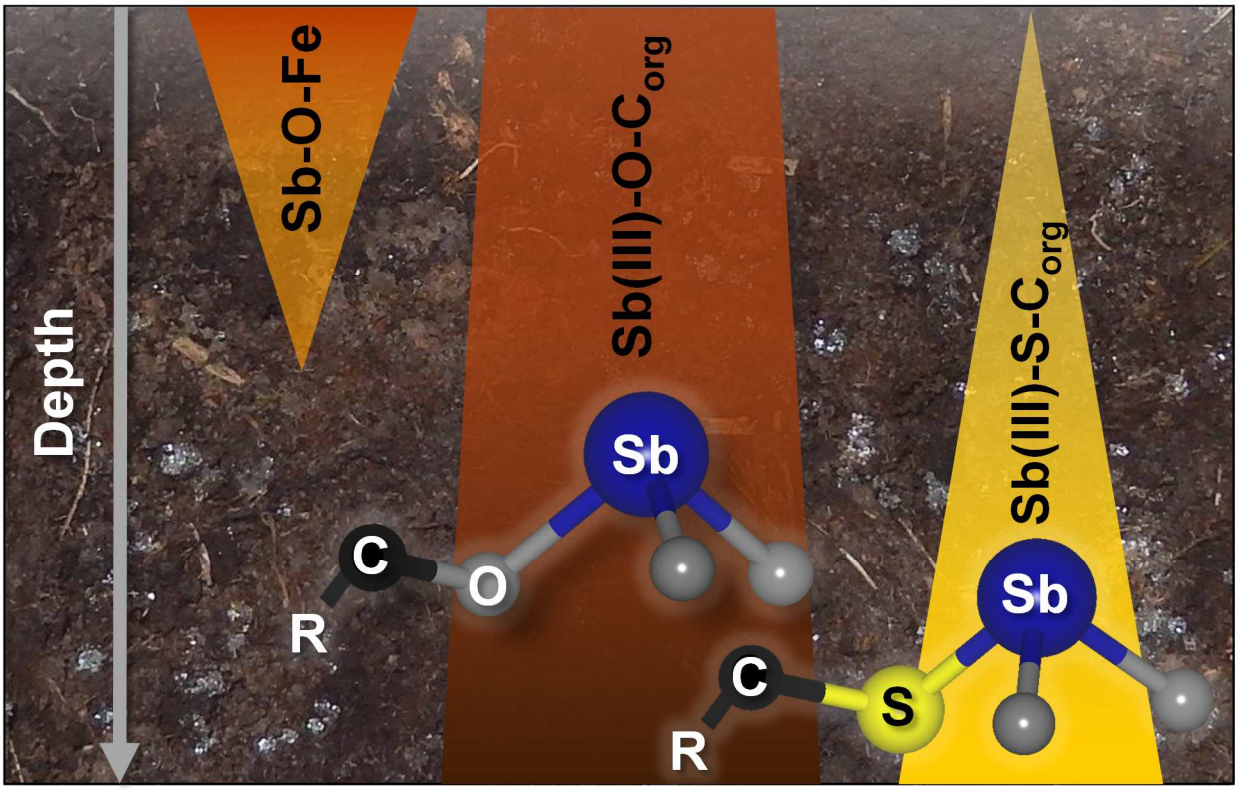

37
38
39

INTRODUCTION

Wetlands span more than 6% of the global ice-free land area[1] and among those, peatlands, with ~3% land cover, are the dominant group of wetlands.[2] Next to important ecological functions regarding long-term carbon storage, niche for threatened animal and plant species or regulation of the water budget, peatlands are increasingly recognized as sinks for potentially toxic trace metal(loid)s[3-7] and therefore are an important factor controlling surface water and groundwater quality.

A potentially toxic trace element, which has only received increasing attention during the last decades due to increased mining activities[8,9] as well as increased industrial use[10-12] and proposed similar toxicity to arsenic[13,14], is antimony (Sb). Antimony is a redox-active trace metalloid that prevails, at environmentally relevant pH values, as pentavalent aqueous antimonate ($Sb(OH)_6^-$) under mostly oxic and as trivalent aqueous antimonite ($Sb(OH)_3$) under mostly anoxic conditions.[15]

The natural Sb background concentrations in soils and sediments (<10 mg kg^{-1})[12,16] as well as in surface and pore waters (<1 µg L^{-1})[12] are commonly low, however, anthropogenically impacted environments like shooting-range soils or mining impacted soils can reach Sb concentrations up to several thousand mg kg^{-1}, thereby jeopardizing water resources.[17,18]

Further, accumulation of Sb in peatlands or other wetlands rich in solid natural organic matter (NOM) has been reported in recent years.[16,19-26] Two main pathways of how antimony enters the peatlands or other wetlands have been described: either through atmospheric deposition related to smelter activities[19-22] or directly e.g. through Sb or gold mining, where (pre-purified) mining water gets in contact with wetland soils.[16,24,25]

Here, two mechanisms have mostly been discussed for Sb retention. In shallow layers, where water is still oxic and abundant (oxyhydr)oxides of iron (Fe) or manganese are thermodynamically stable, typically oxidized Sb(V) can be retained on the (oxyhydr)oxide surfaces by formation of innerspheric complexes.[17,27]

With increasing depth due to increasing water content and eventually saturation (anoxic conditions), iron and manganese (oxyhydr)oxides undergo reductive dissolution[28,29] typically accompanied by an initial release of associated Sb.[30] A (microbially catalyzed) reduction[31,32] of Sb(V) to Sb(III) can then facilitate reaction with (biogenic) dissolved sulfide to form authigenic amorphous Sb-S precipitates at low to neutral pH values, which has been considered as a main Sb retention mechanism in the anoxic zones of wetlands.[16,25,31,33]

As a third way of Sb retention, we recently demonstrated with purified model peat NOM and by use of X-ray absorption spectroscopy that Sb(III) can form innerspheric complexes with O-bearing groups of peat NOM.[34] Further, increased thiol content in the peat NOM lead to increased Sb(III) complexation via thiol bonds, demonstrating the higher affinity of Sb(III) to those organic moieties. These results suggest that retention of Sb in anoxic layers of peatlands may also be facilitated by direct complexation of Sb(III) with solid peat NOM and high dissolved sulfide concentrations for Sb(III) sulfide precipitation are not necessarily required.

Indeed, dissolved sulfide concentrations in peatlands are commonly low[35-38] since the (biogenically) produced sulfide can be effectively incorporated into NOM as organic thiols[35,39], often the dominant sulfur species in such systems.[40] Further, several studies have already observed a strong association of Sb with solid NOM,[19-23,25] however, direct spectroscopic evidence for Sb binding to NOM from field samples was lacking.

In order to study the fate of anthropogenic Sb in peatlands impacted by mine water, we exemplarily determined the speciation of Sb as well as Fe and S, elements which often govern Sb biogeochemistry, in three profiles in a mine water impacted treatment peatland located in Finnish Lapland (Figure SI-1). The peatland (~17 ha) has been used for purification of pre-treated drainage water from open pits and underground gold mining and is in operation since 2006. Inflow to the peatland contains high loads of SO_4^{2-}, N, P and various metals and metalloids including Ni, As and Sb. Previous water analyses showed that Sb inflow concentrations were higher than the outflow concentrations, indicating that the peatland sequesters Sb.[16]

The objective of our study was hence to identify the dominant Sb solid-phase binding mechanisms in natural peat impacted by Sb containing mine water. Therefore, we geochemically characterized three peat profiles distributed over the peatland and analyzed selected peat samples by means of bulk Sb, Fe and S X-ray absorption spectroscopy.

Additionally, we used aqueous Sb speciation supplemented by thermodynamic calculations to further investigate Sb sequestration potential.

MATERIALS AND METHODS

Field Work. Peat profiles were sampled at three different locations along the water flow from near to the inflow to close to the outflow of the peatland (B1-B3, Figure SI-1). Location and field-site characteristics have been published before[16] and are summarized in the **Supporting Information**.

Peat pore water was sampled using equilibrium dialysis samplers (peepers) of type Hesslein[41,42] with a length of 80 cm and 5 cm resolution for the first 20 cm and 10 cm resolution from 20 to 80 cm. Peepers were installed in mid-May 2017 for four weeks to guarantee equilibrium conditions.[42] After collection, peepers were transported in Argon-filled bags to avoid redox-induced sample change to the close-by provisional field laboratory. There, pore water was sampled from the chambers of the peepers using syringe and needle. Samples were filtered (0.2 µm, cellulose acetate), stabilized and cooled or analyzed directly on-site.

Within a radius of ~30 cm to each peeper location, peat cores were sampled up to a maximum sampling depth of 80 cm using a Russian Peat Borer. Then, the peat cores were separated into 10 cm sections to match the pore water information obtained from peepers. Each depth section was immediately transferred to a separate argon filled glass bottle (50 mL), purged again with argon before closing and screwed with PTFE-sealed screw caps. Afterwards, the bottles were transported under refrigerated conditions on ice packs to the laboratory in Bayreuth, where they were immediately processed within an anaerobic glove bag (Coy, N_2/H_2 95/5 % (v/v), pO_2 <1 ppm). Details about the pore water and peat core sampling procedure can be found in the **Supporting Information.**

Aqueous-Phase Analyses. Redox potential, pH and electrical conductivity were determined directly after sampling the chambers using a special set-up to minimize redox changes and to handle small sample volumes (Figure SI-2). Dissolved sulfide was quantified using the methylene

blue method[43] and ferrous iron (Fe(II)) as well as total dissolved iron (Fe(tot)) were measured using the phenanthroline method[44] with a portable photometer (LASA 100, Dr. Lange) at wavelengths of 605 nm and 480 nm, respectively. Total aqueous Sb and S concentrations were determined by inductively coupled plasma mass-spectrometry (ICP-MS, XSeries2, Thermo-Fisher) in stabilized pore water samples (0.44% (v/v) H_2O_2 (Fisher Scientific), 0.78 % (v/v) HNO_3 (Kraft)). Aqueous Sb speciation of samples stabilized in 0.2% (v/v) HCl (Kraft) was carried out with an anion-exchange chromatography (AEC, ICS-3000, Dionex; PRPX-100, 250 x 4.1 mm, 10 µm, Hamilton) coupled to an ICP-MS using an isocratic elution with 10 m NH_4NO_3, 10 mM $NH_4H_2PO_4$, and 500 mg/L Na_2-EDTA at a flow rate of 1.0 mL/min. Calibration standards were prepared from potassium antimonyl tartrate sesquihydrate (Acros) and potassium hexahydroxoantimonate (Fluka) stock solutions.

Solid-Phase Analyses. Back in the laboratory in Bayreuth, the peat of each depth section was homogenized in its bottle inside a glovebag and transferred into a 50 mL polyethylene tube (Sarstedt) for freeze-drying.[45] One part of freeze-dried peat was stored anoxically, dry and dark until solid-phase analyses and another part was milled to <45 µm in a ball mill (MM2000, Retsch) for total element determination. Total Sb content was determined by ICP-MS and total Fe and S contents by inductively coupled plasma optical emission spectrometry (ICAP 6300 Duo View, Thermo-Fisher) after microwave digestion (MARS Xpress, CEM) using a 5:3 ratio of 30% H_2O_2 and 65% HNO_3. To get an overview of the down-core distributions of many other major and trace elements, ground peat samples were analyzed by an energy dispersive X-ray fluorescence spectrometer (XEPOSTM, Spectro X Lab) together with a NIST 2711 certified reference material. Total C content was analyzed with a TOC analyzer (multi N/C 2100, Analytik Jena).

Selected peat samples were examined by scanning electron microscopy (SEM) using a Leo Gemini 1530 (Carl Zeiss, Germany) with a Schottky emitter and elemental composition analysis was conducted by energy-dispersive X-ray spectrometry (EDS, Oxford X-Max 20, Oxford Instruments). Therefore, selected freeze-dried and homogenized peat samples were ground in a mortar, mounted on aluminum specimen stubs and coated with carbon.

For synchrotron measurements at the Stanford Synchrotron Radiation Lightsource (SSRL), Stanford, USA, selected freeze-dried, homogenized and ground peat samples from all three sample locations were filled into aluminum sample holders and sealed with Kapton tape. Thereby, samples were always kept under anoxic conditions until the end of XAS experiments. Bulk Sb *K*-edge (30,491 eV), Fe *K*-edge (7,112 eV), and S *K*-edge (2,472 eV) XAS spectra were collected in fluorescence mode at beamlines 11-2 (Sb), 4-1 (Fe), and 4-3 (S) under cryogenic (10 K, 11-2 and 4-1) or ambient (inert He (<0.1% (v/v) O_2) atmosphere, 4-3) temperatures. The collected Fe *K*-edge X-ray absorption near edge structure (XANES) and extended X-ray absorption fine structure (EXAFS) spectra and Sb *K*-edge EXAFS spectra were analyzed by linear combination fitting (LCF) using Athena[46] after principal component analysis and target-transform testing (PCA-TT) using SIXpack.[47] The Sb *K*-edge EXAFS shell-by-shell fitting analysis was performed in Artemis.[46] Spectral deconvolutions of normalized S *K*-edge XANES spectra were done in Athena.[59] Details on all XAS measurements, data reduction, and analyses are provided in the **Supporting Information.**

RESULTS AND DISCUSSION

General Geochemical Parameters and Vertical Element Distributions. Geochemical on-site parameters revealed a slightly acidic to circumneutral pH (5.8-7.4) and oxic to sub-oxic redox conditions (148-454 mV). Both pH and redox potential decreased with increasing depth in the peat profiles (Table SI-2). Electrical conductivity remained almost constant across the profile closest to the inflow (B1; 2.0 ±0.2 mS cm^{-1}) but decreased with increasing depth in the other profiles. High total aqueous S concentrations (10.4±2.3 mmol L^{-1}, Table SI-2) thereby mainly contributed to the electrical conductivity (Figure SI-3) of the peatland and originated from oxidation of sulfide ores to aqueous sulfate (Table SI-1) during the mining process.[16]

Down-core distributions of total solid Sb, S, Fe and C_{org} are illustrated in Figure 1 and distributions of additional major and trace elements are displayed in Table SI-3. Antimony contents ranged from <0.1 to 2.2 mmol kg^{-1} ($\bar{x}$=0.6 mmol kg^{-1}). They were highest close to the peat surface in all profiles and decreased with increasing depth. Iron exhibited a similar distribution pattern to Sb, whereas the contents of S only slightly decreased and the contents of C_{org} slightly increased with depth by maintaining minimum Fe:Sb, S:Sb and C_{org}:Sb molar ratios of 64, 136 and 17,000, respectively.

Total aqueous Sb in surface waters was highest close to the inflow (B1, 1,566 nmol L^{-1}) and only slightly decreased towards the outflow (B3) to 1,439 nmol L^{-1}. Within peat profiles, total aqueous Sb concentrations ranged from 63 to 2,275 nmol L^{-1} ($\bar{x}$=480 nmol L^{-1}) and showed a similar pattern as for solid-phase Sb (Figure 1a). However, aqueous Sb concentrations in B2 were low (max. 380 nmol L^{-1}) throughout the profile and solid-phase Sb contents were elevated in the first 40 cm, suggesting high Sb retention within the peat (Figure 1).

Iron and Sulfur Solid-Phase Speciation. Solid-phase Fe speciation results from Fe *K*-edge XANES and EXAFS spectra of peat samples as well as Fe reference compounds identified as peat compounds during spectra evaluation are illustrated in Figure 2 and summarized in Table SI-10 and 11. Identification of major Fe species and quantification of their respective fractions within peat samples was done by means of PCA-TT followed by LCF analysis of XANES and EXFAS spectra. Firstly, the number of potential Fe species within the peat samples was elucidated by PCA and suitable reference compounds were identified with TT out of a comprehensive library (Table SI-7 and 9). Afterwards, LCF analysis was performed and the significant number of fitted components for the respective sample spectra was confined with the Hamilton test. Best LCF fit models for XANES and EXAFS spectra thereby were almost identical, suggesting overall realistic fit results (Table SI-10 and 11).

Solid-phase Fe speciation revealed up to 43% of Fe occurring as phyllosilicates in the upper peat layers which was additionally supported by SEM-EDS results (Figure SI-3, Table SI-4). Phyllosilicates most probably originated from the underlying bedrock of greenschist[48] and presumably entered the peatland via the inflow of treated mine drainage water. Organic Fe(III) complexes (up to 47%) generally decreased with increasing peat depth, whereas Fe(II)-NOM complexes (up to 48%) increased. Organic Fe(III) complexes can form in substantial amounts, even at neutral pH values, in oxic layers of environments with abundant NOM such as peatlands and can even dominate over Fe (oxyhydr)oxides.[49] Although, PCA-TT analyses of EXAFS spectra suggested that ferrihydrite, lepidocrocite, and/or schwertmannite, all representatives of Fe (oxyhydr)oxides, were suitable reference compounds (Table SI-7 and 9), no Fe (oxyhydr)oxides could be fitted to the sample spectra in significant percentages (>10%). Nonetheless, the existence of at least small amounts of Fe (oxyhydr)oxides could be demonstrated by SEM-EDS, where a

213 particle of most likely lepidocrocite, an Fe (oxyhydr)oxide forming through oxidation of aqueous
214 Fe(II) e.g. induced through an oscillating water table, was observed. (citation)
215 Further, the formation of substantial amounts of Fe(II)-NOM complexes in deeper peat layers
216 suggests that solid NOM plays an active role in (re)-sequestering aqueous Fe(II)[50] (Table SI-2)
217 after (microbially catalyzed) reductive dissolution of Fe (oxyhydr)oxides[28], Fe containing
218 phyllosilicates[51,52] or Fe(III)-NOM complexes.
219 Additionally, with increasing depth and subsequently increasing reducing conditions (Table SI-
220 2), the presence of (authigenic) iron mono sulfides (FeS) increased and dominated the Fe
221 speciation in deeper peat layers (up to 71%). Here, our SEM-EDS analyses also added supporting
222 information about presence of FeS precipitates (Figure SI-3, Table SI-4).
223 Sulfur *K*-edge XANES spectra of selected peat samples are shown in Figure 3 and the results
224 from Gaussian deconvolutions, which represent s → p transitions of major S fractions, are
225 illustrated in Figures SI-5-6 and Tables SI-12-13. The S XANES spectra could generally be
226 divided into two main spectral regions. The first region ("reduced S") with white line energies
227 <2774.5 eV corresponded to inorganic (mono) sulfide, exocyclic/elemental S and heterocyclic S.
228 The second region with white line energies >2780.6 eV ("oxidized S") was characterized as
229 sulfonate S and sulfate S. The region with energies in between (2774.5< x <2780.6 eV) and with
230 only minor importance in our samples (max. 14% of fitted fractions) was summarized as
231 "intermediate oxidized S" which was deconvoluted as sulfoxide S and sulfone S fractions and was
232 likely to be overestimated due to post-edge absorption features of reduced S species.[53]
233 Validity of the Fe and S solid-phase speciation results was verified by comparing fitted FeS
234 fractions (from Fe XANES and EXAFS analyses) and inorganic (mono) sulfide fractions (from S
235 XANES analyses) and deviations were found to be reasonable ($\overline{x}$=43±32%, Table SI-14).

Two main down-core trends were observed for S in each peat profile. The fractions of oxidized S, which dominated all spectra at the peat surfaces (27-41%), decreased with increasing peat depth to 20-27%, whereas the reduced S fractions increased and dominated deep peat layers (66-71%) (Figure 3, Table SI-13). The oxidized S fraction hereby was mainly represented through sulfate S (Figure SI-5), which most likely originated from the high sulfate inflow concentrations (Table SI-1) and at least partly precipitated as artificial calcium sulfate ($CaSO_4$) during the freeze-drying process of peat samples (Figures SI-4 and SI-6, Table SI-4) due to the low solubility of $CaSO_4$ (K_{SP} = 4.36).

Within reduced S fractions, the exocyclic/elemental S fraction, often represented as thiol-S in organic-rich sediments,[40] prevailed in deep peat layers (32-35%) followed by inorganic (mono) sulfides (20-27%) (Figure SI-6). Both are suitable entities for antimonite sequestration.[34,54] Formation of organic thiol groups and/or inorganic (mono) sulfides in deeper peat layers often is linked to (microbial) sulfate reduction[40], although in all measured samples, dissolved sulfide concentrations were low (max. 3.6 µmol L^{-1}, Table SI-2).

Overall, our solid-phase speciation results demonstrate that independent of the electronic state of Fe and S, which followed the oxic-anoxic down-core redox gradient, NOM plays an important role as reaction partner or binding site in the peatland and thus may also be an important factor for Sb retention.

Antimony Solid-Phase Speciation. Figure 4 shows Sb *K*-edge XANES and EXAFS spectra from selected peat samples as well as Sb reference compounds identified as peat compounds during spectra evaluation. The edge positions of XANES spectra varied between 30,492.5 and 30,493.8 eV and showed a clear decreasing trend with increasing peat depth within each peat profile (Figure

4a). Edge positions fell between Sb(III) and Sb(V) reference compounds indicating mixtures of Sb species (Figure 4e).

Similar to Fe solid-phase analyses, we used PCA-TT followed by LCF of EXAFS spectra to elucidate the coordination environment of Sb in peat samples. Best LCF models revealed the presence of five major Sb species, specifically Sb(III) and Sb(V) inorganically associated with Fe, Sb(III) associated with O-bearing groups of NOM (Sb(III)-O-C_{org}), Sb(III) associated with thiol groups of NOM (Sb(III)-S-C_{org}) and an amorphous Sb(III) sulfide phase. All LCF results are illustrated in Figure 4d and summarized in Table SI-18.

Several similar Sb down-core trends were observed in all peat profiles. With fractions of 22-24%, Sb(V) associated with Fe solely existed in the uppermost peat layers and only in profile B1 at 40 cm, a significant fraction of Sb(III) associated with Fe (18%) could be fitted; despite the general correlation between down-core total Sb and Fe contents and a minimum molar Fe:Sb ratio of 64 in all profiles described before (Figure 1). A similar observation was made by Mikutta and Rothwell[55] in British peat bogs, where a correlation between As and Fe contents was observed, but contribution of As-Fe associations was only moderate.

The exact Sb-O-Fe binding mechanisms hereby remain elusive, since our best-fit references "Sb(III)/(V)-ferrihydrite" have to be considered as proxies for Fe coordination environments such as the before described Fe (oxyhydr)oxides, Fe containing phyllosilicates and/or Fe(II)/Fe(III)-NOM complexes. The Fe(II)/Fe(III)-NOM complexes can provide Fe as bridging cation for ternary complex formation (as e.g. described for As[56-58]). Despite up to 100% of Fe-NOM complexes found, no ternary As-Fe-OM complex formation was observed in an EXAFS study on As binding in peatlands before.[55] These results suggest that ternary Sb-Fe-NOM complexes tend to be of minor importance, which is underlined by the fact that up to 62% (Figure 2) of Fe-NOM complexes were

found in the studied peatland while a maximal of only 25% of Sb was associated with Fe (Figure 4).

With 63-100% ($\bar{x}$=82%), organically coordinated Sb(III) was found to be the dominant fraction in every peat profile and across all depths (Figure 4, Table SI-18). Hereby, Sb(III) associated with O-bearing groups, abundant in peat NOM, revealed the highest percentages (52-64%, $\bar{x}$=60%). High affinity of antimonite to O-bearing groups of microbial extracellular polymeric substances and solid model peat NOM has just recently been shown.[34,59] However, Sb-C distances in Besold et al.[34] were considerably longer (2.90 Å) than the fitted Sb-C distance of our best-fit reference compound "Sb(III) complexed with Aldrich humic acid" (2.83 Å, Figure SI-8, Table SI-19), but both lay in the range of published Sb-C distances of ~2.85 - ~2.92 Å[60,61], indicative for phenol groups.

Regardless of the fact that we could observe an Sb-C(O) backscatter feature in the Fourier transforms of our sample spectra, we were not able to model a significant Sb-C(O) contribution within our shell-by-shell fit approach, probably due to partly overlaying Sb-S resonances (Figure SI-9). Nevertheless, systematic exclusion of this Sb(III)-O-C reference in test fits lead to clearly worse fit qualities (Table SI-20) and therefore suggest the Sb(III)-O-C reference to be a true component in the studied peat samples.

The LCF results further revealed that with increasing depth, Sb(III) was increasingly bound to thiol groups of NOM (14-37%, $\bar{x}$=22%) and therefore showed a similar down-core pattern as the exocyclic/elemental S fraction fitted to the S XANES spectra as described before (Figure SI-6). In one case an Sb(III) sulfide phase was fitted with 37% to the spectrum of sample B2 60 cm (Figure 4, Table SI-18). Shell-by-shell fitting of Sb-S distances of 2.46±0.01 Å for thiol-bonds and a fitted Sb-S distance of 2.48 Å for the Sb(III) sulfide containing sample confirmed our LCF results

(Figure SI-10 and Table SI-21). Formation of Sb(III)-S surface associations on FeS phases in peat samples (Figure 2) with similar Sb-S distances of 2.46 Å[54] cannot be fully excluded, however, in a previous study[34] we demonstrated that spectral differences between organic thiols and inorganic Sb(III) on FeS phases exist and during our LCF analysis we found no best fit model where the latter significantly contributed to or improved fit quality (Table SI-18). Interestingly, sample B2 60 cm, where the Sb(III) sulfide phase was found and redox potential was lowest (148 mV), also exhibited the highest contribution of inorganic (mono) sulfides within all S XANES spectra (Figure SI-6), indicating required natural conditions for inorganic Sb-S sequestration in our system.

In summary, our Sb speciation results suggest that organically complexed Sb dominates solid-phase Sb in all peat samples even in the presence of Fe phases and formation of thiol-bound Sb with increasing depth correlates with the thiol group content in peat.

Geochemical Factors Leading to Low Sb Purification Efficiency in the Studied Peatland. Our Sb solid-phase speciation results showed high affinities of Sb to organic functional groups of peat and recent results from Besold et al.[34] moreover demonstrated high sorption capacities of model peat NOM for Sb under reducing conditions, both indicating a high Sb removal potential of peatlands. However, the long-term purification efficiency in the investigated peatland is low (~30%).[16]

The peatland received high Sb inflow concentrations (1884±876 nmol L^{-1}) over the past ten years. High hydrological loads (41±20 mm d^{-1}) (Table SI-1), which lead to mostly water overflow conditions (~20 cm), may be considered as a suitable explanation for low Sb retention.[62] However, geochemical factors also have to be regarded in order to obtain a comprehensive understanding of this system.

Aqueous antimony speciation of surface waters revealed solely the presence of antimonate and only little increase of antimonite with increasing depth was found in profile B2 (Figure SI-11). Aqueous thio-antimony species using another chromatographic method (not shown) were not detected in any of the profiles. Pourbaix diagrams for the Sb-O-H-S system were calculated with PhreePlot using peatland Sb and S concentrations (Figure SI-12). Plotting respective pH-E_h-values from B1-B3 (Table SI-2) in the Pourbaix diagram confirmed that all surface water samples were located in the predominance field of antimonate. Further, all samples from profile B1 and upper layers of B3 were located in the predominance field of antimonate and only samples from B2 and low B3 layers ranged around the boundary between antimonate and antimonite, generally supporting results from aqueous Sb speciation.

Thus, both thermodynamic calculations and aqueous Sb speciation show that the majority of aqueous Sb was present in form of the negatively charged antimonate oxyanion ($Sb(OH)_6^-$).

Natural organic matter has a net negative surface charge which further increases with increasing thiol group content and increasing pH[63], thus, probably leading to electrostatic repulsions with the negatively charged antimonate at pH>4.[64,65] This repulsion is considered as main factor for overall low Sb retention.[66]

Additionally, dissolved organic matter in the peatland, though not analyzed, may have a negative effect on antimonate sorption capacity to metal (oxyhydr)oxides (e.g. ferrihydrite and/or lepidocrocite) by competitive sorption and through organic-mineral interactions. These interactions in turn can lead to a loss of sorption sites as well as steric and electrostatic repulsions towards other species like arsenate or antimonate[67-69] and may partly explain the low affinity of antimonate to Fe surfaces in our system. This effect is probably supported by the relatively high pH of ~7 in the peatland and points of zero charge of naturally existing (oxyhydr)oxides being

usually lower than the ones in synthetic precipitates (e.g. 5.3-7.5 vs. 8.0-8.3 for ferrihydrite[61,62]). Therefore, lowered outer-sphere complexation of Sb with metal (oxyhydr)oxides through less protonated surface sites is also suspected.[70]

While geochemical reasons for low antimonate retention were elucidated before, an efficient (microbially catalyzed) transformation of antimonate to antimonite in the peatland would certainly increase total Sb retention on phyllosilicates or (oxyhydr)oxides as well as on peat NOM surfaces.[34,70] Slightly acidic inflow conditions (pH 5-6) then could probably further increase Sb(III) thiol-binding or even lead to Sb(III) sulfide precipitation as described in the literature for arsenic.[38]

The low concentrations of aqueous antimonite (Figure SI-11) on the one hand, but almost only Sb(III) species found during Sb solid-phase speciation (Figure 4) on the other hand, hereby suggest a high reactivity of Sb(III) towards peat surfaces.[25] Therefore, antimonate reduction kinetics probably are a key limiting factor in this system. Low reduction rates may explain, together with the high Sb inflow concentrations, why antimonate dominates aqueous Sb speciation in most peat layers despite sulfate-reducing conditions, as verified by FeS formation (Figure 2 and Figure 3). Almost identical sulfate inflow-outflow concentrations (Table SI-1) and low dissolved sulfide concentration in peat profiles (Table SI-2) further show that the peatland chemistry was substantially governed by the inflow water chemistry.

In sum, the high hydrological load, which leads to short water residence times and preferential flow in the peatland[62] in combination with the high antimonate inflow concentrations as well as the cold climate in Finnish Lapland (-0.5°C mean annual temperature)[16], which probably results in lowered microbial activity and therefore reduced antimonate and sulfate reduction rates, are considered as main factors hindering efficient Sb retention.

373 **Environmental Implications.** Peatlands and other wetlands have been reported to act as
374 geochemical sinks for Sb before,[16,19-25] but direct spectroscopic evidence elucidating the Sb
375 coordination environments of natural peat was missing. Our results therefore add important
376 information about the biogeochemistry of Sb in (mine water impacted) peatlands, supported by
377 solid-phase spectroscopic data of Fe and S, elements which often govern the geochemistry of Sb.
378 Our molecular findings reveal that Sb was not primarily coordinated to Fe phases, even close to
379 peat surfaces, as implied by the macroscopic correlation between Sb and Fe, but rather that organic
380 functional groups of abundant peat NOM are the main controlling factor for Sb, Fe, and S
381 biogeochemistry in peatlands. Our results therefore highlight the complex interplay of metal(loid)s
382 such as Sb in peatlands, where NOM not only serves as carbon source for Sb redox dynamics[71] or
383 competing molecule (DOM) for Sb sorption on mineral surfaces[17], but also as effective sorption
384 site for Sb sequestration.
385 The innerspheric binding of antimonite to phenol and/or thiol groups may therefore also explain
386 why Sb showed similar distribution pattern as organically-bound lead in ombotrophic peat profiles
387 after atmospheric deposition.[19-21] The post-depositional immobility of Sb over long time
388 periods[20,21] thus let us speculate about the long-term stability of these Sb-NOM associations.
389 Solid-phase Sb speciation results further imply that abundant peat organic phenol and thiol
390 groups are key binding sites in natural wetland samples for reduced antimonite and demonstrate
391 their high importance in comparison to Sb sulfide precipitation. Although important for Sb
392 sequestration, Sb(III) sulfide phases seem not to form primarily under sub-oxic conditions and low
393 dissolved sulfide concentrations, as they prevailed in the studied peatland.

ASSOCIATED CONTENT

Supporting Information

Field site characteristics and sampling, Additional general geochemical characterization, Scanning Electron Microscopy/Energy Dispersive X-Ray Spectroscopy analyses and results, Iron solid-phase speciation analyses and results, Sulfur solid-phase speciation analyses and results, Antimony solid-phase speciation analyses and results, Aqueous Sb speciation results

AUTHOR INFORMATION

Corresponding Author

* Phone: +49-921-553999; Fax: +49-921-552334; email: b.planer-friedrich@uni-bayreuth.de

Notes

The authors declare no competing financial interest.

ACKNOWLEDGMENTS

This work was funded by the German Research Foundation Grant PL 302/20-1, a PhD student short-time stipend to Stanford University for Johannes Besold (German Academic Exchange Service, DAAD 57314604) as well as a DAAD mobility grant (DAAD 57315737) to Britta Planer-Friedrich. Sampling in Finland was supported by a BayIntAn mobility grant (BayIntAn_UBT_2017_23) awarded to Britta Planer-Friedrich. We acknowledge help for field-sampling from Constantin Heitzer and for SEM-EDS analyses from Dorothea Wiesner (BGI Bayreuth). Antimony, iron and sulfur *K*-edge XAS experiments were performed at the Stanford Synchrotron Radiation Lightsource (SSRL), a Directorate of SLAC National Accelerator

Laboratory and an Office of Science User Facility operated for the US Department of Energy, Office of Science, Office of Basic Energy Sciences under Contract No. DE-AC02-76SF00515. We would like to thank Ryan Davis for his support in using beamline 11-2 and 4-1 as well as Matthew Latimer and Eric Nelson for help at beamline 4-3.

422 References

423 1. Reddy, K.; DeLaune, R. D., Biogeochemistry of Wetlands: Science and Applications. In
424 CRC Press Boca Raton 2008.

425 2. Rydin, H.; Jeglum, J. K., Peatlands around the world. In *The Biology of Peatlands*, Oxford
426 University Press: Oxford, 2006; p 216−238.

427 3. Reddy, K. R.; DeLaune, R. D., Metals/Metalloids. In *Biogeochemistry of Wetlands:*
428 *Science and Applications*, CRC Press–Taylor & Francis: Boca Raton, Florida, 2008.

429 4. Mikutta, C.; Langner, P.; Bargar, J. R.; Kretzschmar, R., Tetra- and Hexavalent Uranium
430 Forms Bidentate-Mononuclear Complexes with Particulate Organic Matter in a Naturally
431 Uranium-Enriched Peatland. *Environ. Sci. Technol.* **2016,** *50*, (19), 10465-10475.

432 5. Skyllberg, U.; Xia, K.; Bloom, P. R.; Nater, E. A.; Bleam, W. F., Binding of Mercury(II)
433 to Reduced Sulfur in Soil Organic Matter along Upland-Peat Soil Transects. *J. Environ. Qual.*
434 **2000,** *29*, (3), 855-865.

435 6. Gündoğan, R.; Acemioğlu, B.; Alma, M. H., Copper (II) adsorption from aqueous solution
436 by herbaceous peat. *J. Colloid Interface Sci.* **2004,** *269*, (2), 303-309.

437 7. González A, Z. I.; Krachler, M.; Cheburkin, A. K.; Shotyk, W., Spatial Distribution of
438 Natural Enrichments of Arsenic, Selenium, and Uranium in a Minerotrophic Peatland, Gola di
439 Lago, Canton Ticino, Switzerland. *Environ. Sci. Technol.* **2006,** *40*, (21), 6568-6574.

440 8. Brown, T. J.; Idoine, N. E.; Raycraft, E. R.; Shaw, R. A.; Deady, E. A.; Rippingale, J.;
441 Bide, T.; Wrighton, C. E.; Rodley, J., Word Mineral Production 2008-2012. *British Geological*
442 *Survey* **2014**.

443 9. Brown, T. J.; Idoine, N. E.; Raycraft, E. R.; Shaw, R. A.; Hobbs, S. F.; Everett, P.; Deady,
444 E. A.; Bide, T., World Mineral Production 2012-2016. *British Geological Survey* **2018**.

445 10. Krachler, M.; Emons, H.; Zheng, J., Speciation of antimony for the 21st century: promises
446 and pitfalls. *TrAC, Trends Anal. Chem.* **2001,** *20*, (2), 79-90.

447 11. Scheinost, A. C.; Rossberg, A.; Vantelon, D.; Xifra, I.; Kretzschmar, R.; Leuz, A.-K.;
448 Funke, H.; Johnson, C. A., Quantitative antimony speciation in shooting-range soils by EXAFS
449 spectroscopy. *Geochim. Cosmochim. Acta* **2006,** *70*, (13), 3299-3312.

450 12. Filella, M.; Belzile, N.; Chen, Y.-W., Antimony in the environment: a review focused on
451 natural waters: I. Occurrence. *Earth Sci. Rev.* **2002,** *57*, (1), 125-176.

452 13. Zhang, D.; Pan, X.; Mu, G.; Wang, J., Toxic effects of antimony on photosystem II of
453 Synechocystis sp. as probed by in vivo chlorophyll fluorescence. *J. Appl. Phycol.* **2010,** *22*, (4),
454 479-488.

455 14. Verdugo, M.; Ogra, Y.; Quiroz, W., Mechanisms underlying the toxic effects of antimony
456 species in human embryonic kidney cells (HEK-293) and their comparison with arsenic species.
457 *J. Toxicol. Sci.* **2016,** *41*, (6), 783-792.

458 15. Filella, M.; Belzile, N.; Chen, Y.-W., Antimony in the environment: a review focused on
459 natural waters: II. Relevant solution chemistry. *Earth Sci. Rev.* **2002,** *59*, (1), 265-285.

460 16. Palmer, K.; Ronkanen, A.-K.; Kløve, B., Efficient removal of arsenic, antimony and nickel
461 from mine wastewaters in Northern treatment peatlands and potential risks in their long-term use.
462 *Ecol. Eng.* **2015,** *75*, 350-364.

17. Hockmann, K.; Schulin, R., Leaching of Antimony from Contaminated Soils. In *Competitive sorption and transport of heavy metals in soils*, 2012.

18. Wilson, S. C.; Lockwood, P. V.; Ashley, P. M.; Tighe, M., The chemistry and behaviour of antimony in the soil environment with comparisons to arsenic: A critical review. *Environ. Pollut.* **2010,** *158*, (5), 1169-1181.

19. Shotyk, W.; Krachler, M.; Chen, B., Antimony in recent, ombrotrophic peat from Switzerland and Scotland: Comparison with natural background values (5,320 to 8,020 14C yr BP) and implications for the global atmospheric Sb cycle. *Global Biogeochem. Cycles* **2004,** *18*, (1), 1-13.

20. Cloy, J. M.; Farmer, J. G.; Graham, M. C.; MacKenzie, A. B., Retention of As and Sb in Ombrotrophic Peat Bogs: Records of As, Sb, and Pb Deposition at Four Scottish Sites. *Environ. Sci. Technol.* **2009,** *43*, (6), 1756-1762.

21. Cloy, J. M.; Farmer, J. G.; Graham, M. C.; MacKenzie, A. B.; Cook, G. T., A comparison of antimony and lead profiles over the past 2500 years in Flanders Moss ombrotrophic peat bog, Scotland. *J. Environ. Monit.* **2005,** *7*, (12), 1137-1147.

22. Rothwell, J. J.; Taylor, K. G.; Chenery, S. R. N.; Cundy, A. B.; Evans, M. G.; Allott, T. E. H., Storage and Behavior of As, Sb, Pb, and Cu in Ombrotrophic Peat Bogs under Contrasting Water Table Conditions. *Environ. Sci. Technol.* **2010,** *44*, (22), 8497-8502.

23. Arsic, M.; Teasdale, P. R.; Welsh, D. T.; Johnston, S. G.; Burton, E. D.; Hockmann, K.; Bennett, W. W., Diffusive Gradients in Thin Films Reveals Differences in Antimony and Arsenic

Mobility in a Contaminated Wetland Sediment during an Oxic-Anoxic Transition. *Environ. Sci. Technol.* **2018,** *52*, (3), 1118-1127.

24. Warnken, J.; Ohlsson, R.; Welsh, D. T.; Teasdale, P. R.; Chelsky, A.; Bennett, W. W., Antimony and arsenic exhibit contrasting spatial distributions in the sediment and vegetation of a contaminated wetland. *Chemosphere* **2017,** *180*, 388-395.

25. Fawcett, S. E.; Jamieson, H. E.; Nordstrom, D. K.; McCleskey, R. B., Arsenic and antimony geochemistry of mine wastes, associated waters and sediments at the Giant Mine, Yellowknife, Northwest Territories, Canada. *Appl. Geochem.* **2015,** *62*, 3-17.

26. Bennett, W. W.; Hockmann, K.; Johnston, S. G.; Burton, E. D., Synchrotron X-ray absorption spectroscopy reveals antimony sequestration by reduced sulfur in a freshwater wetland sediment. *Environ. Chem.* **2017,** *14*, (6), 345-349.

27. Tighe, M.; Lockwood, P.; Wilson, S., Adsorption of antimony(v) by floodplain soils, amorphous iron(iii) hydroxide and humic acid. *J. Environ. Monit.* **2005,** *7*, (12), 1177-1185.

28. Schwertmann, U., Solubility and dissolution of iron oxides. *Plant Soil* **1991,** *130*, (1), 1-25.

29. Petrunic, B. M.; MacQuarrie, K. T. B.; Al, T. A., Reductive dissolution of Mn oxides in river-recharged aquifers: a laboratory column study. *J. Hydrol.* **2005,** *301*, (1), 163-181.

30. Hockmann, K.; Lenz, M.; Tandy, S.; Nachtegaal, M.; Janousch, M.; Schulin, R., Release of antimony from contaminated soil induced by redox changes. *J. Hazard. Mater.* **2014,** *275*, 215-221.

503 31. Kulp, T. R.; Miller, L. G.; Braiotta, F.; Webb, S. M.; Kocar, B. D.; Blum, J. S.; Oremland,
504 R. S., Microbiological Reduction of Sb(V) in Anoxic Freshwater Sediments. *Environ. Sci.*
505 *Technol.* **2014,** *48*, (1), 218-226.

506 32. Nguyen, V. K.; Lee, J.-U., Antimony-Oxidizing Bacteria Isolated from Antimony-
507 Contaminated Sediment – A Phylogenetic Study. *Geomicrobiol. J.* **2015,** *32*, (1), 50-58.

508 33. Webb; McGinness; Lappin-Scott, Metal removal by sulphate-reducing bacteria from
509 natural and constructed wetlands. *Journal of Applied Microbiology* **1998,** *84*, (2), 240-248.

510 34. Besold, J., Antimonite complexation with thiol and carboxyl/phenol groups of peat organic
511 matter. *Environ. Sci. Technol.* **2019**.

512 35. Spratt, H. G.; Morgan, M. D., Sulfur cycling in a cedar-dominated, freshwater wetland.
513 *Limnol. Oceanogr.* **1990,** *35*, (7), 1586-1593.

514 36. Steinmann, P.; Shotyk, W., Ion chromatography of organic-rich natural waters from
515 peatlands IV. Dissolved free sulfide and acid-volatile sulfur. *J. Chromatogr. A* **1995,** *706*, (1), 287-
516 292.

517 37. Shotyk, W., Review of the inorganic geochemistry of peats and peatland waters. *Earth Sci.*
518 *Rev.* **1988,** *25*, (2), 95-176.

519 38. Besold, J.; Biswas, A.; Suess, E.; Scheinost, A. C.; Rossberg, A.; Mikutta, C.; Kretzschmar,
520 R.; Gustafsson, J. P.; Planer-Friedrich, B., Monothioarsenate Transformation Kinetics
521 Determining Arsenic Sequestration by Sulfhydryl Groups of Peat. *Environ. Sci. Technol.* **2018,**
522 *52*, (13), 7317-7326.

523 39. Yu, Z.-G.; Göttlicher, J.; Steininger, R.; Knorr, K.-H., Organic sulfur and organic matter
524 redox processes contribute to electron flow in anoxic incubations of peat. *Environ. Chem.* **2016,**
525 *13*, (5), 816-825.

526 40. Werne, J. P.; Hollander, D. J.; Lyons, T. W.; Sinninghe Damsté, J. S., Organic sulfur
527 biogeochemistry: Recent advances and future research directions. *Special Paper Geological*
528 *Society of America* **2004,** *379*, (135).

529 41. Hesslein, R. H., An in situ sampler for close interval pore water studies. *Limnol. Oceanogr.*
530 **1976,** *21*, (6), 912-914.

531 42. Steinmann, P.; Shotyk, W., Sampling anoxic pore waters in peatlands using "peepers" for
532 in situ-filtration. *Fresenius' Journal of Analytical Chemistry* **1996,** *354*, (5), 709-713.

533 43. Cline, J. D., Spectrophotometric determination of hydrogen sulfide in natural waters.
534 *Limnol. Oceanogr.* **1969,** *14*, (3), 454-458.

535 44. Fortune, W.; Mellon, M., Determination of iron with o-phenanthroline: a
536 spectrophotometric study. *Industrial & Engineering Chemistry Analytical Edition* **1938,** *10*, (2),
537 60-64.

538 45. Ji, Y.; Sarret, G.; Schulin, R.; Tandy, S., Fate and chemical speciation of antimony (Sb)
539 during uptake, translocation and storage by rye grass using XANES spectroscopy. *Environ. Pollut.*
540 **2017,** *231*, 1322-1329.

541 46. Ravel, B.; Newville, M., ATHENA, ARTEMIS, HEPHAESTUS: data analysis for X-ray
542 absorption spectroscopy using IFEFFIT. *J. Synchrotron Radiat.* **2005,** *12*, (4), 537-541.

543 47. Webb, S. M., SIXpack: a graphical user interface for XAS analysis using IFEFFIT. *Phys.*
544 *Scr.* **2005,** *2005*, (T115), 1011.

545 48. Wyche, N. L.; Eilu, P.; Koppström, K.; Kortelainen, V. J.; Niiranen, T.; Välimaa, J.,
546 Chapter 5.2 - The Suurikuusikko Gold Deposit (KittilÄ Mine), Northern Finland. In *Mineral*
547 *Deposits of Finland*, Maier, W. D.; Lahtinen, R.; O'Brien, H., Eds. Elsevier: 2015; pp 411-433.

548 49. Karlsson, T.; Persson, P., Coordination chemistry and hydrolysis of Fe(III) in a peat humic
549 acid studied by X-ray absorption spectroscopy. *Geochim. Cosmochim. Acta* **2010,** *74*, (1), 30-40.

550 50. Catrouillet, C.; Davranche, M.; Dia, A.; Bouhnik-Le Coz, M.; Marsac, R.; Pourret, O.;
551 Gruau, G., Geochemical modeling of Fe(II) binding to humic and fulvic acids. *Chem. Geol.* **2014,**
552 *372*, 109-118.

553 51. Lee, J.-H.; Fredrickson, J. K.; Kukkadapu, R. K.; Boyanov, M. I.; Kemner, K. M.; Lin, X.;
554 Kennedy, D. W.; Bjornstad, B. N.; Konopka, A. E.; Moore, D. A.; Resch, C. T.; Phillips, J. L.,
555 Microbial Reductive Transformation of Phyllosilicate Fe(III) and U(VI) in Fluvial Subsurface
556 Sediments. *Environ. Sci. Technol.* **2012,** *46*, (7), 3721-3730.

557 52. Wu, T.; Shelobolina, E.; Xu, H.; Konishi, H.; Kukkadapu, R.; Roden, E. E., Isolation and
558 Microbial Reduction of Fe(III) Phyllosilicates from Subsurface Sediments. *Environ. Sci. Technol.*
559 **2012,** *46*, (21), 11618-11626.

560 53. Manceau, A.; Nagy, K. L., Quantitative analysis of sulfur functional groups in natural
561 organic matter by XANES spectroscopy. *Geochim. Cosmochim. Acta* **2012,** *99*, (Supplement C),
562 206-223.

563 54. Kirsch, R.; Scheinost, A. C.; Rossberg, A.; Banerjee, D.; Charlet, L., Reduction of
564 antimony by nano-particulate magnetite and mackinawite. *Mineral. Mag.* **2008,** *72*, (1), 185-189.

565 55. Mikutta, C.; Rothwell, J. J., Peat Bogs as Hotspots for Organoarsenical Formation and
566 Persistence. *Environ. Sci. Technol.* **2016,** *50*, (8), 4314-4323.

567 56. Mikutta, C.; Frommer, J.; Voegelin, A.; Kaegi, R.; Kretzschmar, R., Effect of citrate on
568 the local Fe coordination in ferrihydrite, arsenate binding, and ternary arsenate complex formation.
569 *Geochim. Cosmochim. Acta* **2010,** *74*, (19), 5574-5592.

570 57. Hoffmann, M.; Mikutta, C.; Kretzschmar, R., Arsenite Binding to Natural Organic Matter:
571 Spectroscopic Evidence for Ligand Exchange and Ternary Complex Formation. *Environ. Sci.*
572 *Technol.* **2013,** *47*, (21), 12165-12173.

573 58. Hiemstra, T.; van Riemsdijk, W. H., Adsorption and surface oxidation of Fe(II) on metal
574 (hydr)oxides. *Geochim. Cosmochim. Acta* **2007,** *71*, (24), 5913-5933.

575 59. Zhou, L.; Li, A.; Ma, F.; Yang, J.; Pi, S.; Tang, A., Sb(V) Reduced to Sb(III) and More
576 Easily Adsorbed in the Form of Sb(OH)3 by Microbial Extracellular Polymeric Substances and
577 Core–Shell Magnetic Nanocomposites. *ACS Sustainable Chemistry & Engineering* **2019**.

578 60. Horley, G. A.; Mahon, M. F.; Molloy, K. C.; Venter, M. M.; Haycock, P. W.; Myers, C.
579 P., Structures of Sb(OC6H3Me2-2,6)3 and Sb(OEt)5·NH3: The First Authenticated Monomeric
580 Sb(OR)n (n = 3, 5). *Inorg. Chem.* **2002,** *41*, (6), 1652-1657.

581 61. Tella, M.; Pokrovski, G. S., Antimony(III) complexing with O-bearing organic ligands in
582 aqueous solution: An X-ray absorption fine structure spectroscopy and solubility study. *Geochim.*
583 *Cosmochim. Acta* **2009,** *73*, (2), 268-290.

584 62. Khan, U. A.; Kujala, K.; Planer-Friedrich, B.; Räisänen, M. L.; Ronkanen, A.-K., Seasonal
585 and long-term trends of antimony retention and mobilization in boreal treatment peatlands. *Sci.*
586 *Total Environ.* **submitted 06.05.2019**.

587 63. Catrouillet, C.; Davranche, M.; Dia, A.; Bouhnik-Le Coz, M.; Pédrot, M.; Marsac, R.;
588 Gruau, G., Thiol groups controls on arsenite binding by organic matter: New experimental and
589 modeling evidence. *J. Colloid Interface Sci.* **2015,** *460*, (Supplement C), 310-320.

590 64. Li, X.; Reich, T.; Kersten, M.; Jing, C., Low Molecular Weight Organic Acid
591 Complexation Affects Antimony(III) Adsorption by Granular Ferric Hydroxide. *Environ. Sci.*
592 *Technol.* **2019**.

593 65. Tella, M.; Pokrovski, G. S., Antimony(V) complexing with O-bearing organic ligands in
594 aqueous solution: an X-ray absorption fine structure spectroscopy and potentiometric study.
595 *Mineral. Mag.* **2008,** *72*, (1), 205-209.

596 66. Verbeeck, M.; Warrinnier, R.; Gustafsson, J. P.; Thiry, Y.; Smolders, E., Soil organic
597 matter increases antimonate mobility in soil: An Sb(OH)6 sorption and modelling study. *Appl.*
598 *Geochem.* **2019**.

599 67. KAISER, K.; GUGGENBERGER, G.; HAUMAIER, L.; ZECH, W., Dissolved organic
600 matter sorption on sub soils and minerals studied by 13C-NMR and DRIFT spectroscopy. *Eur. J.*
601 *Soil Sci.* **1997,** *48*, (2), 301-310.

602 68. Filius, J. D.; Meeussen, J. C. L.; Lumsdon, D. G.; Hiemstra, T.; van Riemsdijk, W. H.,
603 Modeling the binding of fulvic acid by goethite: the speciation of adsorbed FA molecules.
604 *Geochim. Cosmochim. Acta* **2003,** *67*, (8), 1463-1474.

605 69. Gustafsson, J. P., Arsenate adsorption to soils: Modelling the competition from humic
606 substances. *Geoderma* **2006,** *136*, (1), 320-330.

607 70. Leuz, A.-K.; Mönch, H.; Johnson, C. A., Sorption of Sb(III) and Sb(V) to Goethite:
608 Influence on Sb(III) Oxidation and Mobilization. *Environ. Sci. Technol.* **2006,** *40*, (23), 7277-
609 7282.

610 71. Borch, T.; Kretzschmar, R.; Kappler, A.; Cappellen, P. V.; Ginder-Vogel, M.; Voegelin,
611 A.; Campbell, K., Biogeochemical Redox Processes and their Impact on Contaminant Dynamics.
612 *Environ. Sci. Technol.* **2010,** *44*, (1), 15-23.

613

614

615

616

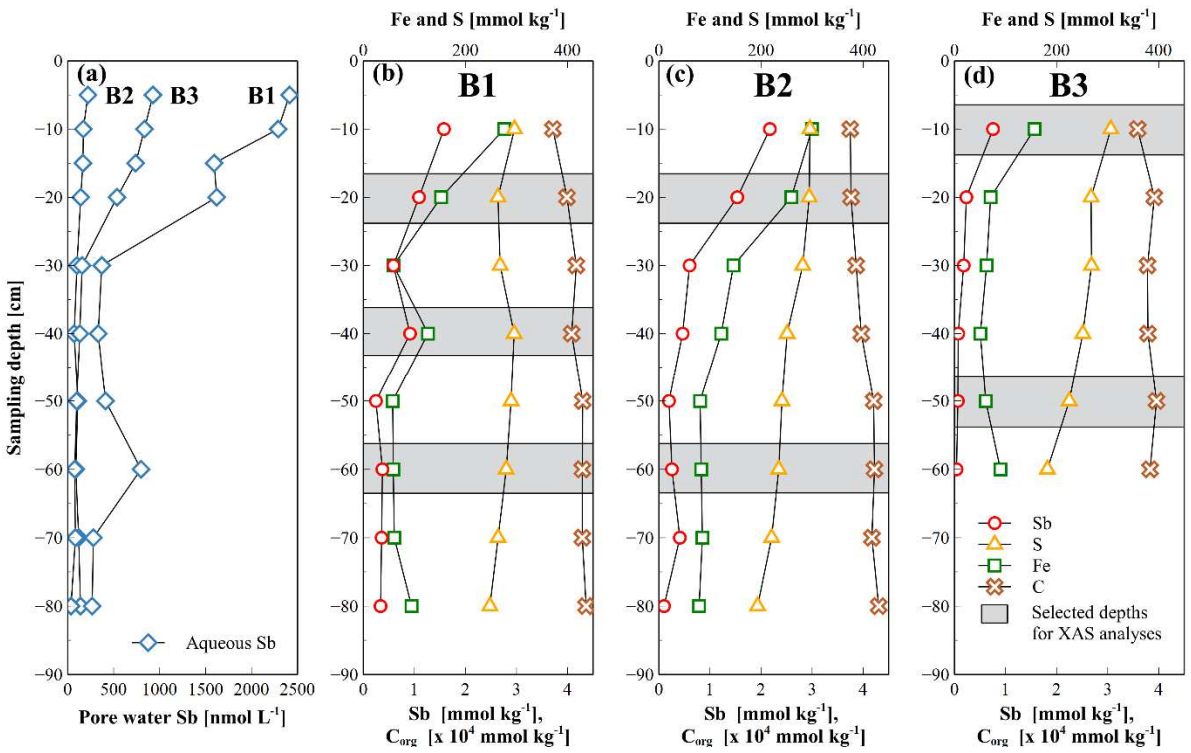

Figure 1: Vertical element distributions in peat samples for sampling points B1-B3. Total aqueous Sb concentrations (a) and down core contents of Sb, S, Fe, and C_{org} for sampling points B1-B3, respectively (b-d). Element contents are given on dry-weight basis. Total C represents organic C (C_{org}) only as absence of carbonates was tested with 10% HCl. Depth resolution for aqueous Sb: 0-20 cm: 5 cm; 20-80 cm: 10 cm. Solid-phase element distribution resolution: 10 cm, whereby e.g. 10 cm depth means an integrated sample from 0-10 cm. At sampling location B3, solid-phase sampling was only possible down to 60 cm. Please note that the scales differ between upper and lower x-axes.

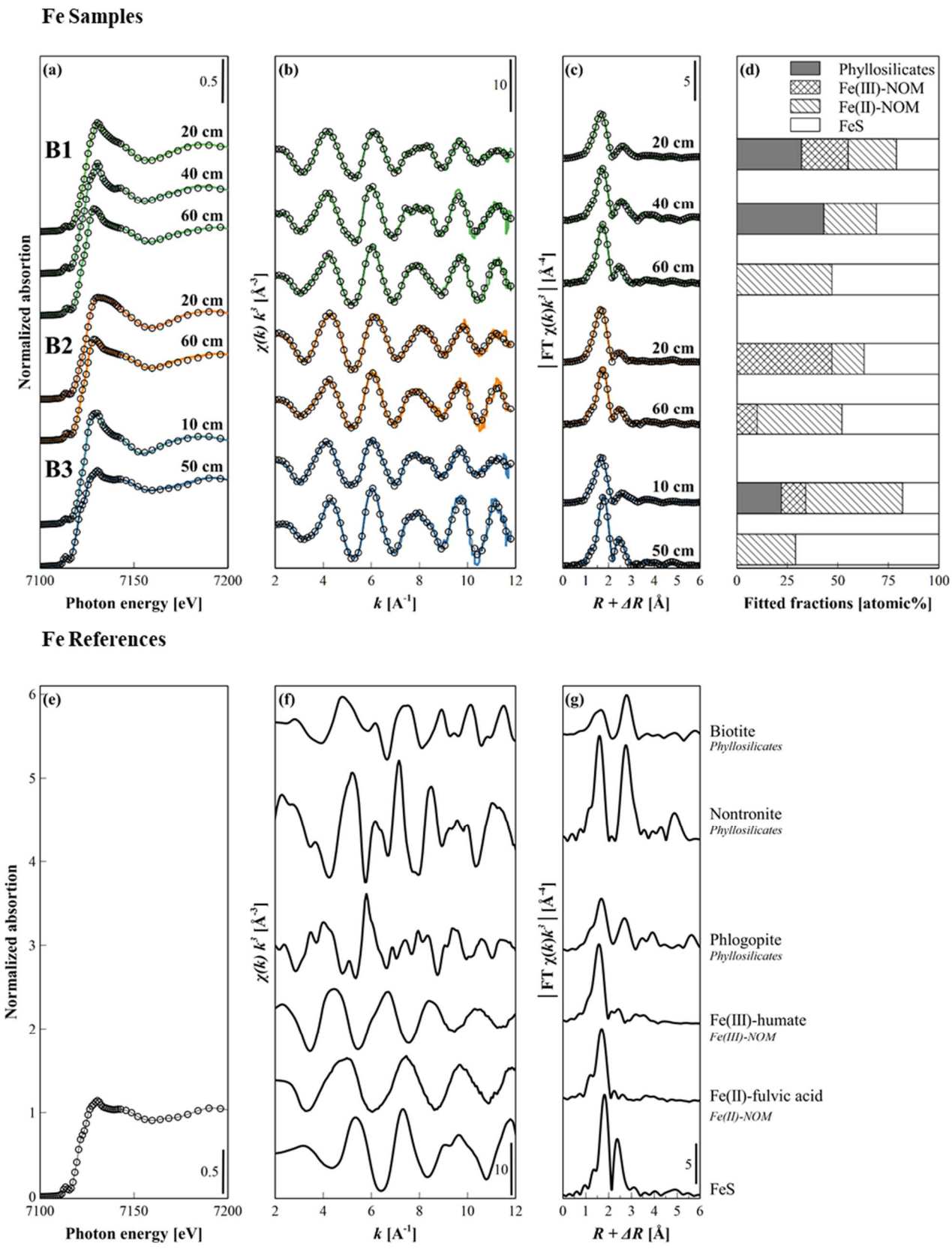
Fe Samples
(a)
0.5
B1
20 cm
40 cm
60 cm
B2
20 cm
60 cm
B3
10 cm
50 cm
Normalized absorption
7100
7150
7200
Photon energy [eV]
(b)
10
χ(k) k³ [Å⁻³]
2
4
6
8
10
12
k [A⁻¹]
(c)
5
20 cm
40 cm
60 cm
20 cm
60 cm
10 cm
50 cm
| FT χ(k)k³ | [Å⁻⁴]
0
1
2
3
4
5
6
R + ΔR [Å]
(d)
Phyllosilicates
Fe(III)-NOM
Fe(II)-NOM
FeS
0
25
50
75
100
Fitted fractions [atomic%]
Fe References
(e)
0.5
Normalized absorption
Photon energy [eV]
(f)
10
χ(k) k³ [Å⁻³]
k [A⁻¹]
(g)
5
| FT χ(k)k³ | [Å⁻⁴]
R + ΔR [Å]
Biotite
Phyllosilicates
Nontronite
Phyllosilicates
Phlogopite
Phyllosilicates
Fe(III)-humate
Fe(III)-NOM
Fe(II)-fulvic acid
Fe(II)-NOM
FeS

631

Figure 2: Normalized Fe *K*-edge XANES spectra (a, e), k^3-weighted Fe *K*-edge EXAFS spectra (b, f) and their corresponding Fourier-transform (FT) magnitudes (c, g) of selected peat samples and Fe references. Best linear combination fits of Fe *K*-edge EXAFS peat spectra (d). The Fe EXAFS spectra are illustrated here as LCF results since similarities of XANES spectra for different iron sulfides and oxides do not appear for EXAFS spectra and make EXAFS LCF a more powerful method for Fe solid-phase speciation. Detailed results about Fe *K*-edge XANES and EXAFS best fit models can be found in Table SI-10 and 11. Individual fractions were constrained to values between 0 and 100%, the sum of fractions was not constrained. Linear combination fits of the samples are shown as black circles. Fit references: Phyllosilicates=∑(Biotite, Nontronite, Phlogopite). Fe(III)-NOM = Fe(III)-humate. Fe(II)-NOM = Fe(II)-DOM (Suwannee River Fulvic Acid (SRFA)). FeS = FeS from microbial sulfate reduction.

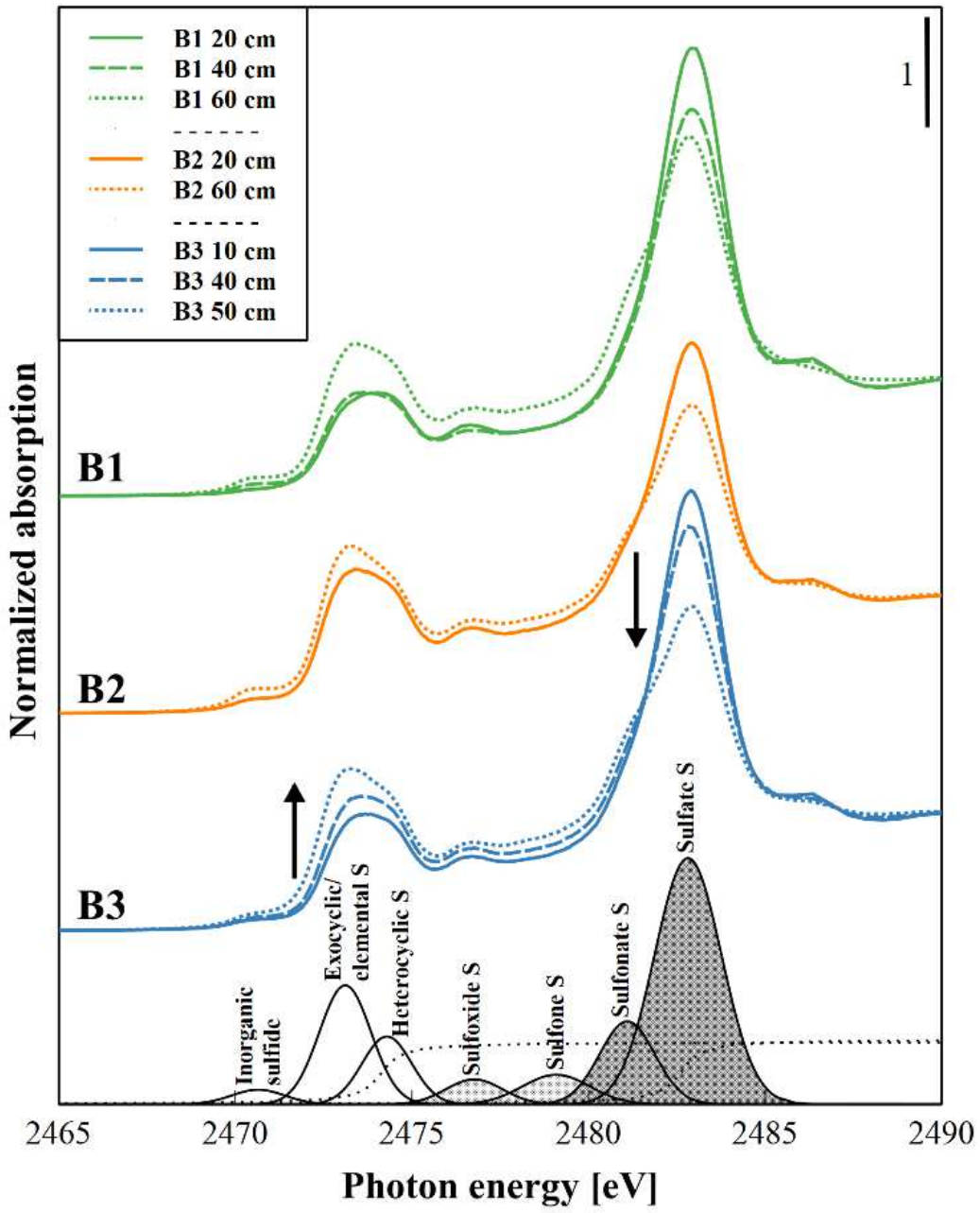

646

647 Figure 3: Sulfur solid-phase speciation of selected peat samples from sampling points B1-B3. The
648 normalized S *K*-edge XANES spectra of peat are plotted as a function of sampling depth. Spectral
649 decomposition is illustrated as an example for sample B3 50 cm (with offset from the other
650 spectra). The two arctan functions are shown as dotted lines and the Gaussian functions as straight
651 lines correspond to reduced S (oxidation states –II to + I; no shading): inorganic (mono) sulfide,

652 exocyclic/elemental S, heterocyclic S; intermediate oxidized S (oxidation states >+I to + III; light
653 grey shading): sulfoxide S, sulfone S and oxidized S (oxidation states >+III to +VI; dark grey
654 shading): sulfonate S, sulfate S. The experimental data and fit envelopes as well as all fit
655 parameters for every sample can be found in Figure SI-5 and SI-6 as well as Table SI-12 and 13.
656 Please note that the intermediate oxidized fractions (sulfoxide and sulfone S) are likely to be
657 overestimated due to post-edge absorption features of reduced S species.[53]

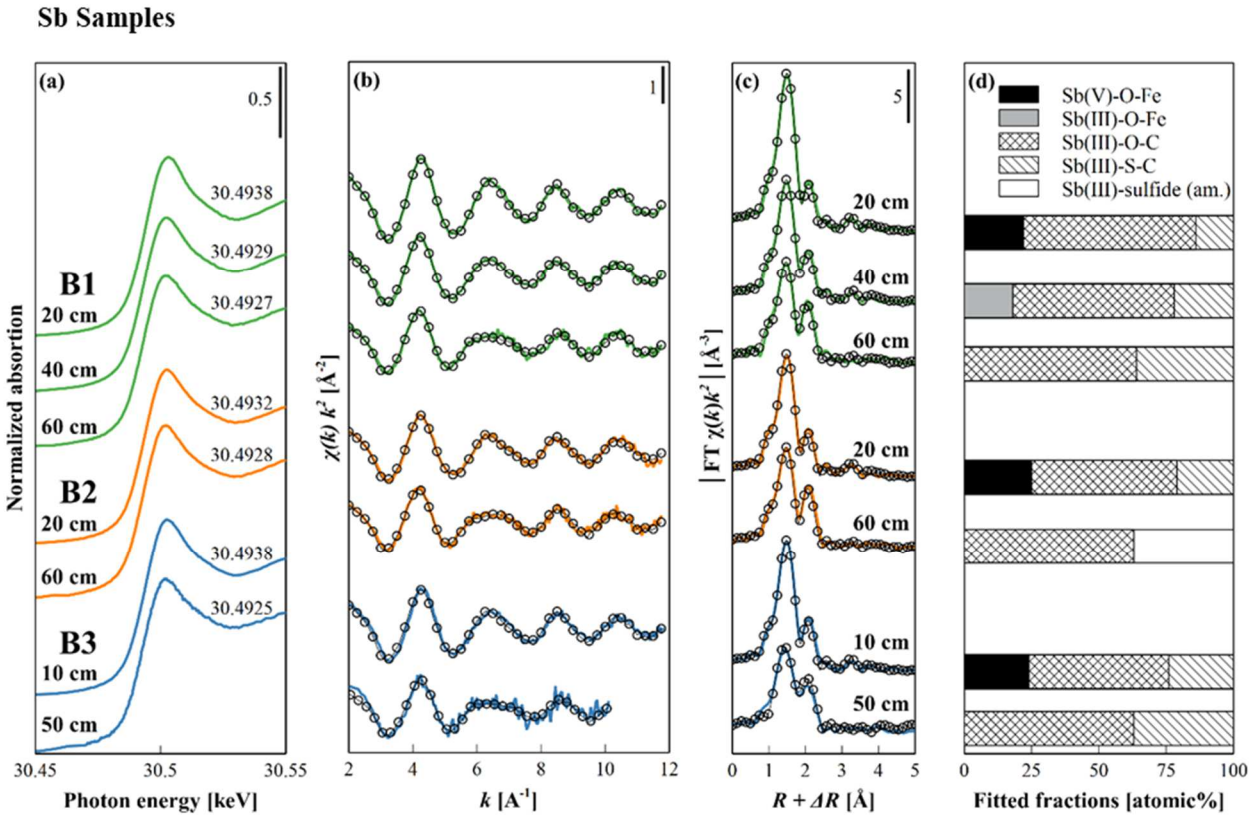
Sb Samples
(a)
0.5
30.4938
30.4929
30.4927
B1
20 cm
40 cm
60 cm
30.4932
30.4928
B2
20 cm
60 cm
30.4938
30.4925
B3
10 cm
50 cm
Normalized absorption
30.45
30.5
30.55
Photon energy [keV]
(b)
1
χ(k) k² [Å⁻²]
2
4
6
8
10
12
k [A⁻¹]
(c)
5
20 cm
40 cm
60 cm
20 cm
60 cm
10 cm
50 cm
| FT χ(k)k² | [Å⁻³]
0
1
2
3
4
5
R + ΔR [Å]
(d)
Sb(V)-O-Fe
Sb(III)-O-Fe
Sb(III)-O-C
Sb(III)-S-C
Sb(III)-sulfide (am.)
0
25
50
75
100
Fitted fractions [atomic%]

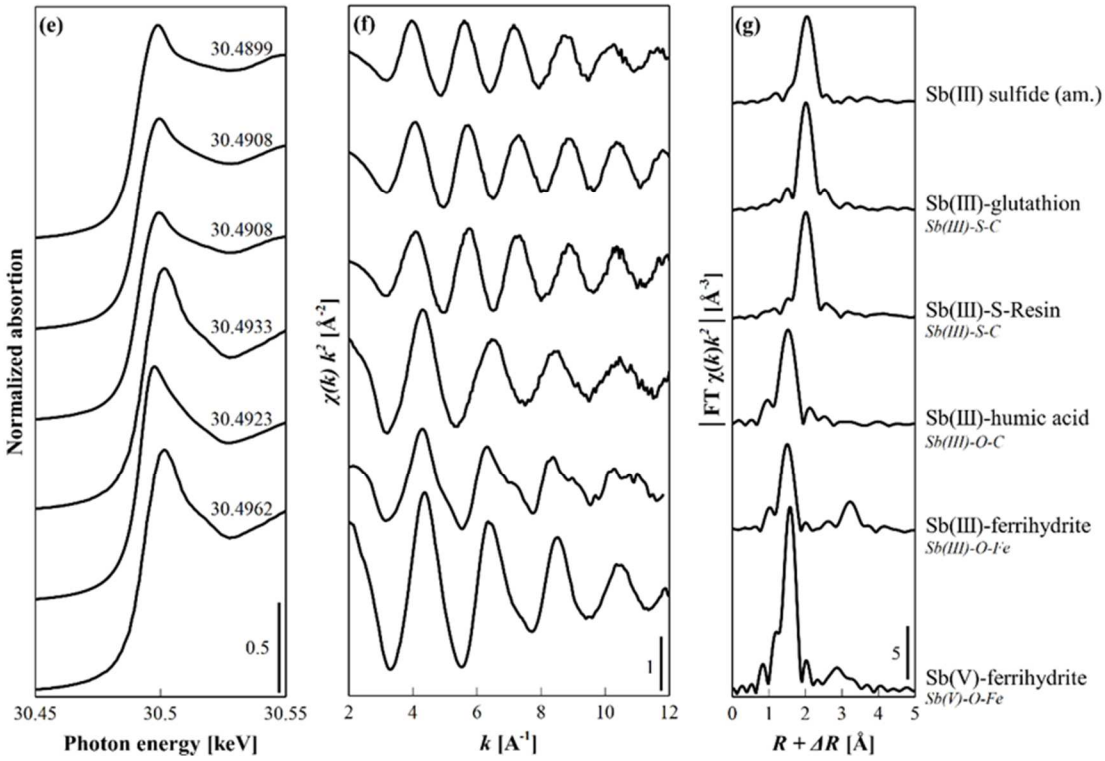
Sb References
(e)
30.4899
30.4908
30.4908
30.4933
30.4923
30.4962
0.5
Normalized absorption
30.45
30.5
30.55
Photon energy [keV]
(f)
1
χ(k) k² [Å⁻²]
2
4
6
8
10
12
k [A⁻¹]
(g)
5
| FT χ(k)k² | [Å⁻³]
0
1
2
3
4
5
R + ΔR [Å]
Sb(III) sulfide (am.)
Sb(III)-glutathion
Sb(III)-S-C
Sb(III)-S-Resin
Sb(III)-S-C
Sb(III)-humic acid
Sb(III)-O-C
Sb(III)-ferrihydrite
Sb(III)-O-Fe
Sb(V)-ferrihydrite
Sb(V)-O-Fe

658

Figure 4: Normalized Sb *K*-edge XANES spectra and their respective edge-energies (keV) (a, e), k^2-weighted Sb *K*-edge EXAFS spectra (b, f) and their corresponding Fourier-transform (FT) magnitudes (c, g) of selected peat samples and Sb references. Best linear combination fits of Sb *K*-edge EXAFS peat spectra (d). Detailed results can be found in Table SI-18. Individual fractions were constrained to values between 0 and 100%, the sum of fractions was not constrained. Linear combination fits of the samples are shown as black circles. Fit references: Sb(V)-O-Fe = Sb(V) adsorbed to ferrihydrite, Sb(III)-O-Fe = Sb(III) adsorbed to ferrihydrite, Sb(III)-O-C= Sb(III) complexed with phenol groups of OM (Sb(III)-Aldrich humic acid), Sb(III)-S-C = Sb(III) complexed with thiol groups of OM: sum of Sb(III)-thiol resin (Ambersep GT74) and Sb(III)-glutathione), Sb(III) sulfide (am.) = amorphous Sb(III) sulfide.